Synchronized oscillations, traveling waves, and jammed clusters induced by steric interactions in active filament arrays

Raghunath Chelakkot[a‡], Michael F. Hagan[b], Arvind Gopinath[c*]

Autonomous active, elastic filaments that interact with each other to achieve cooperation and synchrony underlie many critical functions in biology. The mechanisms underlying this collective response and the essential ingredients for stable synchronization remain a mystery. Inspired by how these biological entities integrate elasticity with molecular motor activity to generate sustained and stable oscillations, a number of synthetic active filament systems have been developed that mimic oscillations of these biological active filaments. Here, we describe the collective dynamics and stable spatiotemporal patterns that emerge in such biomimetic multi-filament arrays, under conditions where steric interactions may impact or dominate the collective dynamics. To focus on the effect of steric interactions, we study the system using Brownian dynamics simulations, without considering long-ranged hydrodynamic interactions. The simulations treat each filament as a connected chain of self-propelling colloids. We demonstrate that short-range steric inter-filament interactions and filament roughness are sufficient - even in the absence of inter-filament hydrodynamic interactions - to generate a rich variety of collective spatiotemporal oscillatory, traveling and static patterns. We first study the collective dynamics of two- and three-filament clusters and identify parameter ranges in which steric interactions lead to synchronized oscillations and strongly occluded states. Generalizing these results to large one-dimensional arrays, we find rich emergent behaviors, including traveling metachronal waves, and modulated wavetrains that are controlled by the interplay between the array geometry, filament activity, and filament elasticity. Interestingly, the existence of metachronal waves is non-monotonic with respect to the inter-filament spacing. We also find that the degree of filament roughness significantly affects the dynamics – specifically, filament roughness generates a locking-mechanism that transforms traveling wave patterns into statically stuck and jammed configurations. Our simulations suggest that short-ranged steric inter-filament interactions could combine with complementary hydrodynamic interactions to control the development and regulation of oscillatory collective patterns. Furthermore, roughness and steric interactions may be critical to the development of jammed spatially periodic states; a spatiotemporal feature not observed in purely hydrodynamically interacting systems.

Keywords: Active filaments, Metachronal waves, Oscillations, Jamming

1 Introduction

The emergence of oscillations in single or arrayed elastic filamentous structures, such as the graceful rhythmic movements of ciliary beds, is a common motif in biology[1–5]. A striking example is ciliary arrays in the mammalian respiratory tract, in which individual filaments communicate through direct interactions and through the surrounding fluid to generate metachronal traveling waves crucial for mucociliary clearance. In these systems, emergent collective oscillations and waves are strongly affected by multiple effects, including the elasticity of the underlying filamentous structures, modes of activation due to molecular motors, coupling between neighboring filaments, and boundaries[6–18]. Due to the complexity and many-body nature of these systems, disentangling the contributions of each of these effects to the system dynamics is highly challenging.

Inspired by the manner in which these biological active filamentous carpets integrate elasticity with biological motor activity to generate sustained oscillations, a number of reconstituted or synthetic *active filament* systems have been developed[19–31]. Here activity is imbued either by motors acting externally on filaments to generate elastic forces[19–21], or by using internally propelled filaments constructed of beads that are powered by surface chemical reactions or responses to external fields. At a conceptual level, within this class of synthetic systems, oscillations arise due to the interplay between geometry, filament elasticity, and activity. These oscillatory patterns are mainly due to non-linear buckling instabilities through which active energy pumped into the system is continuously dissipated by viscous dissipation. Mechanisms underlying the onset and sustaining of oscillations in these bio-inspired and biomimetic *synthetic cilia* are thus very different from biological cilia and flagella. However, these simple driving mechanisms generate cilia-like responses, and are thus ideal for use in micron-sized pumping and propelling devices. As a result, instabilities in active filament systems have been the subject of several recent theoretical and computational inquiries. Continuum as well as discrete agent-based models have been used to investigate the emergence of oscillations in single filaments, and coupling-induced synchronization in systems of two rotating filaments[32,33,35–37,40–46].

However, an equally important set of problems – the collective behaviors of many elastic active filaments – have yet to be investigated in detail. In this case, key questions are as follows: First, how do autonomously beating individual filaments alter their oscillatory dynamics in response to interactions with their neighbors? In particular, under what conditions do such systems

[a] *Department of Physics, Indian Institute of Technology Bombay, Mumbai, India.*
[b] *Martin A. Fisher School of Physics, Brandeis University, Waltham, MA, USA.*
[c] *Department of Bioengineering, University of California, Merced, CA, USA*
*Corresponding authors: ‡raghu@phy.iitb.ac.in, *agopinath@ucmerced.edu*
† Electronic Supplementary Material (ESM) available: [details of any supplementary information available should be included here]. See DOI: 00.0000/00000000.

exhibit stationary states characterized by propagating spatiotemporal patterns and waves? Second, how are the properties of filament waveforms regulated by the geometric, elastic, and active aspects of the collective system?

In these low Reynolds number viscous environment characterizing the fluid flows generated by the moving filaments, actively driven, collective systems, two types of inter-filament interactions are expected to play a crucial role in addition to single filament properties such as elasticity and activity. The first type comprises fluid-mediated medium- and long-range elasto-hydrodynamic interactions[47] that alter the viscous drag on filaments and couple to their spatiotemporal response. Recent analytical studies[36–38] have analyzed the onset of synchronization of clusters, arrays, and carpets of active filaments grafted to a rigid impenetrable planar wall. Full multi-filament and filament-wall hydrodynamic interactions were considered using singularity methods built on slender body theory. Stable, oscillatory states in which filaments oscillated with the same frequency with a varying phase angle were determined to bifurcate from a stationary state. Other computational studies and phenomenological models that used the simpler resistivity approximation to treat fluid-mediated interactions[48–52] have also demonstrated that hydrodynamic interactions can lead to stable collective and synchronized responses. Similarly, models for systems of two or more rotating cilia have elucidated the role of hydrodynamic interactions in yielding in-phase or out of phase stable states[53,54]. However, to focus on hydrodynamic effects, many of these studies consider models in which elasticity is neglected or highly simplified and contact (steric) interactions are neglected[51,55]. Moreover, filament roughness is not considered in these systems when the filaments are treated as lines with zero thickness.

The second type of interaction includes short-range effects, such as steric interactions, screened electrostatic interactions, and frictional effects from filament roughness. Recent studies suggest that steric interactions and collective fluid mechanical effects both play important roles in biologically relevant multi-filament arrays, such as in the passive arrayed brush-like structures in the glycocalyx[47] and active ciliary carpets in the mucociliary tract[56]. These studies also identify important roles of surface-attached features and networked structures. For instance, Button *et. al.*[56] proposed a Gel-on-Brush model of the mucus clearance system, in which the periciliary layer is occupied by membrane-spanning mucins and large mucopolysaccharides that are tethered to cilia and microvilli. They hypothesize that the tethered macromolecules produce inter-molecular repulsions, which stabilize the layer against compression by an osmotically active mucus layer.

Here in this article, we use agent-based Brownian Dynamics (BD) simulations to investigate the roles of (non-viscous) steric interactions in emergent collective dynamics in filament clusters. To focus on how steric interactions *enable or hinder synchronized and collective states*, we neglect long-ranged hydrodynamic interactions in our BD simulations. We consider each filament to interact with its neighbors via a steric potential with an interaction length-scale σ that is comparable to, but may differ from, the intrinsic geometric filament thickness — the segment length ℓ_0. By adjusting the ratio of these two scales, we vary the inter-filament interactions between the regimes of *smooth* ($\sigma > \ell_0$) or *rough* filaments ($\sigma = \ell_0$). Thus, we study the combined effects of excluded volume and filament roughness on collective behaviors of active filament arrays. These geometries are directly motivated by colloidal chains comprised of connected self-propelling or activated colloidal spheres that have been studied in recent experiments [22,26]. In some of these systems, the forces animating the colloidal chain are imposed externally by electrical or magnetic fields. In other cases, the beads comprising the chain are each chemically modified such that they self-propel when immersed in a suitable medium. The geometry we study is also relevant to the brush-like structure in mucocilia[56]. The mechanisms by which cilia beat and oscillate are very different from those considered in this work. Nonetheless, at an abstract level, the interplay between activity, elasticity, and dissipation provides the underlying mechanism that enables the initiation and sustainment of stable collective states.

The layout of the article is as follows. We first introduce our computational model for an active filament system in §2; in brief, we analyze small filament clusters (2-3 filaments) or large periodic arrays (300 filaments) immersed in a viscous fluid at constant temperature (Figure 1(a)). Each filament or chain comprises elastically coupled active beads that confer bending and

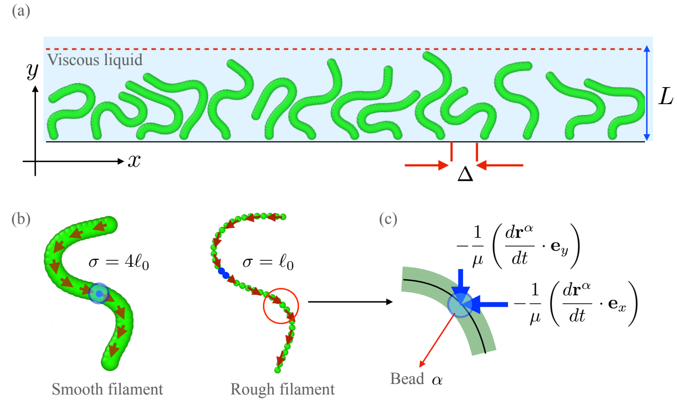

Fig. 1 (a) Typical arrangement of clamped, active filaments in the 1D array used in the simulations. Filaments are arranged along the x axis, with each filament parallel to the y direction in the undeformed state. Each active filament of length L is comprised of $N_{\rm m}$ connected spherical self-propelling beads (discs), with each pair separated by distance Δ in the undeformed state. (b) Schematic of smooth (left) and rough (right) filament structures. Both filaments are comprised of beads with the same bead size (diameter) ℓ_0; however the smooth filament has a larger effective steric interaction lengthscale $\sigma > \ell_0$. The intrinsic elasticity of the filaments (set by the parameters B and $K_{\rm E}$) are the same in both cases; however, the overlapping spheres make the effective surface of the smooth filament less corrugated than that of its rough counterpart. Active tangential compressive forces called follower forces[33] act along the filament backbone and are indicated as red arrows. (c) Schematic of the local hydrodynamics that is included in the model. Segments of the deforming filament experience a viscous drag force as they move. The drag on a test bead that moves with velocity $d\mathbf{r}^\alpha/dt$ is illustrated; the drag force is evaluated using resistive force theory (RFT)[37] and is linear in the *local filament velocity* and proportional to the mobility μ^{-1}. Components normal and tangential to the local filament tangent may be deconstructed into components along the x and y directions as shown in the sketch. Note that hydrodynamic interactions between different filaments are neglected in this model.

extensional rigidities, and is geometrically fixed at one end. The other end is free, and this degree of freedom allows each filament to independently and autonomously oscillate or move in a plane via active buckling instabilities. The intrinsic frequency and amplitude of beating by individual filaments is controlled by the interplay between the filament geometry, elasticity, fluid dissipation, and activity. In the absence of inter-filament interactions, adjacent filaments beat with the same frequency but are generally out of phase. We conclude this section by summarizing results for the dynamics of a single filament, and commenting on the role of hydrodynamics in this context. In §3, we analyze the collective dynamics and emergent steric-driven coupling in small clusters comprising 2 or 3 smooth filaments. Building on this, we then analyze the dynamics of large arrays comprised of smooth filaments in §4. We next probe the effect of filament roughness within the framework of the steric model introduced in §2, by setting $\sigma \approx \ell_0$, resulting in large gradients of the excluded-volume potential between adjacent filaments. Effectively, beads in neighboring filaments interlock as they move, resulting in higher effective friction coefficients and significantly reducing their tangential velocities. This extra friction results in qualitatively different collective dynamics in comparison to the smooth filaments. Furthermore, this modality of collective motion is unique and does not occur in systems for which hydrodynamics is the only mode of inter-filament interactions. The final set of results (§5) explores relaxing the hard constraint (clamped base) by implementing a softer constraint (pivoting base). We conclude in §6 and highlight features that are relevant to previous studies and serve as motivation for future experimental and computational work. We briefly discuss current research that incorporates hydrodynamic interactions and provides an appropriate starting point – when combined with this work – to study the effects of hydrodynamic and steric interactions in tandem in these simple model systems. We note that coupled fluid flow and filament deformation, including non-local coupling due to fluid incompressibility, comprises a complicated highly non-linear problem, especially in the multi-filament systems studied here.

Our investigation of a model system of filaments comprised of self-propelling active units reveals novel and important aspects of emergent dynamics in the limit where short-range repulsive interactions and/or filament roughness dominate. For example, our simulations demonstrate that steric interactions enable and mediate stable oscillatory patterns such as metachronal waves or finite-ranged wavetrains. Depending on the spacing and geometric coupling between neighboring filaments, wavetrains may appear, vanish, and even eventually re-appear. Roughness at the filament scale provides a crucial locking-mechanism that dramatically changes the form and wave-speed of metachronal waves. Moreover, our results demonstrate that the anchoring mechanism at the base of the filament can determine the class of emergent spatiotemporal patterns. Relaxing the strength of the geometric constraint at the base and allowing for flexible pivoting results in jammed static shapes, even though the system itself remains active and dynamic.

2 Computational Model

The active filament carpet/array comprises N two-dimensional active filaments (chains) arrayed uniformly in one dimension along the e_x direction and initially aligned along the e_y direction as illustrated in Figure 1(a). The spacing between the filaments, Δ, is treated as an adjustable parameter in the simulations. We consider sparse carpets comprised of only a few filaments ($N = 2$ and $N = 3$) and then a larger carpet with ($N = 300$) more filaments.

As mentioned earlier, to focus on the role of steric interactions, we do not consider hydrodynamic interactions and the wall only serves to keep the base of the filament fixed. Note that in a system with full hydrodynamic effects included, fluid flow generated by beating filaments will alter the motion of the filament[37,40,41]. In our case, we neglect these induced fluid flows and consider, to leading order, just the Stokes drag in the form of viscous resistive force theory expressions on the beads comprising the filament as they move. Thus each bead in the filament experiences a Stokes drag force antiparallel to the direction of its motion, with a constant of proportionality that depends on the bead size and viscosity of the ambient fluid.

In the following, we introduce potentials that are used to calculate extensional, bending, and steric forces. Dimensional potentials are starred; all potentials are scaled with $k_\mathrm{B}T$ with T the thermodynamic temperature of the ambient fluid.

2.1 Interaction potentials

Each active filament is a collection of N_m polar, active spheres (disks) of effective diameter σ in 2D as shown in Figure 1(b). The coordinate of the α^th sphere is denoted by $\mathbf{r}_\alpha$ and it is connected to the neighbouring spheres of the same filament via extensional and bending potentials as illustrated in Figure 1(c)).

The extensional force between adjacent beads is derived from the total potential U^*_E given by

$$\frac{U^*_\mathrm{E}}{k_\mathrm{B}T} = \frac{\kappa_\mathrm{E}\ell_0^2}{2k_\mathrm{B}T}\sum_{\alpha=1}^{N_\mathrm{m}-1}\Phi^\alpha_\mathrm{E}, \quad \text{where} \quad \Phi^\alpha_\mathrm{E} = \left(\frac{|\mathbf{r}_{\alpha+1}-\mathbf{r}_\alpha|}{\ell_0} - 1\right)^2. \tag{1}$$

The value of κ_E is maintained at a value large enough that the actual distance between each polar particle is nearly ℓ_0, making the chain nearly inextensible. The overall length of the undeformed filament is thus $\ell = (N_\mathrm{m}-1)\ell_0$.

The overall resistance to bending is implemented via a three-body bending potential motivated by the energy for a thin elastic continuous curve in the noise-less limit,

$$U^*_\mathrm{B}(s,t) = \frac{\kappa}{2}\int_0^\ell \mathscr{C}^2(s)\,ds \tag{2}$$

where $\mathscr{C}$ is the curvature measured along the centerline of the curve. We discretize (2) for our model filaments by approximating the curvature at bead α using $\mathscr{C} \approx |d\mathbf{b}/ds| \approx |\mathbf{b}_{\alpha+1} - \mathbf{b}_\alpha|/\ell_0$, where $\mathbf{b}_\alpha = (\mathbf{r}_{\alpha-1} - \mathbf{r}_\alpha)/|\mathbf{r}_\alpha - \mathbf{r}_{\alpha-1}|$ is the unit bond vector that is anti-parallel to the local tangent.

In the continuous limit ($\ell_0 \to 0$, $N_\mathrm{m} \to \infty$, $N_\mathrm{m}\ell_0 \to$ constant), $\mathbf{b}_\alpha$ identifies with the tangent vector $\mathbf{t}$ of the continuous model at arclength $s = \alpha\ell_0$; thus $(\mathbf{b}_{\alpha+1} - \mathbf{b}_\alpha)/\sigma \approx d\mathbf{t}/ds$. Discretizing (2)

Parameter	Interpretation	Scaled value
ℓ_0	Distance between beads	1
$k_B T$	Energy	1
K_E	Extensional modulus	2×10^4
ε	Energy scale in WCA	1
D	Translational diffusivity	1
μ	Mobility	1
σ	Range of WCA potential	4, 1

Table 1 List of parameters held constant in the simulations and their values in dimensionless units.

using $B \equiv \kappa/\ell_0$, we write

$$\frac{U_B^*}{k_B T} = \frac{B}{2k_B T}\sum_{\alpha=1}^{N_m-1}\Phi_B^\alpha, \quad \text{where} \quad \Phi_B^\alpha = \left(\frac{|\mathbf{b}_{\alpha+1}-\mathbf{b}_\alpha|}{\ell_0}\right)^2. \qquad (3)$$

We account for excluded-volume (steric) interactions between beads in neighboring filaments via a short-range repulsive WCA (Weeks-Chandler-Anderson) interaction potential. Here, we have chosen filament lengths and rigidity values such that overlap between beads in the same element does not occur. With $r_{\alpha\beta} \equiv |\mathbf{r}_\alpha - \mathbf{r}_\beta|$ as the distance between a pair of spheres (α,β) belonging to different filaments, the net overall steric potential summed over all segments (beads) is

$$\frac{U_{WCA}^*}{k_B T} = \frac{\varepsilon}{k_B T}\sum_{\alpha=1}^{N_m-1}\Phi_{WCA}^\alpha \qquad (4)$$

where

$$\Phi_{WCA}^\alpha = \sum_{\beta\neq(\alpha,\alpha-1,\alpha+1)} 4\left[\left(\frac{\sigma}{r_{\alpha\beta}}\right)^{12} - \left(\frac{\sigma}{r_{\alpha\beta}}\right)^{6}\right]+1 \qquad (5)$$

if $r_{\alpha\beta} < 2^{\frac{1}{6}}\sigma$ and $u(r)=0$ otherwise. The index β refers to pairs of beads in the same filament as well as in neighboring filaments, thus incorporating all possible steric interactions. In (4), $\varepsilon = k_B T$.

The effect of the steric interactions encoded in the interaction potentials (4) and (5) depends on the softness of the interaction potential and also on the fine structure and roughness of the interacting filament. The former effect is controlled by the power-law exponents in the WCA, while the latter can be varied by changing the ratio ℓ_0/σ. Thus the length-scale σ effectively sets the nature and the scale of the steric excluded volume interactions.

Each disc comprising the filament is self-propelling with a velocity $v_0\mathbf{b}_\alpha$, in the direction of the local tangent $\mathbf{b}_\alpha$ of the filament. This causes local compression, generating *follower* forces of magnitude F that follow the local target of the filament. In the continuous and over-damped limit, this yields a uniform active force per unit length. Since v_0 is a constant for each bead on the filament, the quantity $v_0 = \mu F$ is also constant for each realization and can be interpreted as the magnitude of the active force exerted by each bead. We note that the magnitude of the total force for a straight unbent filament $\sim v_0 N_m/\mu$, so the effective force density $f = F/\ell_0 \sim (v_0 N_m/\mu)/(N_m \ell_0)$.

2.2 Equations of motion

We evolve the position $\mathbf{r}_\alpha$ of each bead α using Brownian dynamics, with the forces accounting for extensional, bending, steric, and thermal effects described above. We render equations dimensionless by scaling quantities as follows. We use ℓ_0 as the unit of length, the diffusive relaxation time ℓ_0^2/D as unit of time, and $k_B T$ as the unit of energy. In the over-damped limit, the equations of motion can be written as

$$\frac{d\mathbf{r}^\alpha}{dt} = -\left(\frac{\mu k_B T}{D}\right)\left(\frac{\kappa_E \ell_0^2}{2k_B T}\boldsymbol{\nabla}\Phi_E^\alpha + \frac{B}{2k_B T}\boldsymbol{\nabla}\Phi_B^\alpha\right)$$
$$-\left(\frac{\mu k_B T}{D}\right)\left(\frac{\varepsilon}{k_B T}\boldsymbol{\nabla}\Phi_{WCA}^\alpha\right)+\left(\frac{\ell_0}{D}\mu F\right)\mathbf{b}_\alpha + \sqrt{2\frac{\ell_0^2}{D}}\,\boldsymbol{\zeta}_\alpha^* \qquad (265)$$

Here $\boldsymbol{\zeta}_\alpha^*$ is a delta-correlated noise with zero mean acting on the disc. With the units of length, time, and energy defined above, the mobility $\mu = D/k_B T = 1$ in dimensionless form. Other parameters in the dimensionless (reduced) units are listed in Table 1. The equations of motion in dimensionless form then reduce to

$$\frac{d\mathbf{r}^\alpha}{dt} = -\left(\frac{\kappa_E}{2}\boldsymbol{\nabla}\Phi_E^\alpha + \frac{B}{2}\boldsymbol{\nabla}\Phi_B^\alpha + \boldsymbol{\nabla}\Phi_{WCA}^\alpha\right) + F\,\mathbf{b}_\alpha + \sqrt{2}\,\boldsymbol{\zeta}_\alpha^* \qquad (6)$$

Interpreting the time derivative in the Ito-Stratanovich sense, we solve Eq. (6) using a time-stepper based on the Euler-Maruyama scheme. Theory[32] shows that the behavior of an isolated active filament depends on a single effective *activity parameter* $\beta \equiv f\ell^3/\kappa$. In our case the *force density* f is related to the force on a bead F by $f = F/\ell_0$, so that

$$\beta \equiv \frac{f\ell^3}{\kappa} = \frac{F(N_m-1)^3}{B}. \qquad (7)$$

2.3 Simulation conditions and parameters

We present simulations for two limiting cases in §3. The first set considers *smooth filaments*, with scaled value $\sigma = 4$; that is, the interaction diameter of the filament is about four times larger than the bond length ℓ_0 (Fig. 1). This prevents the geometric interlocking of neighbouring filaments when they slide past each other, and thus attenuates the sliding resistance due to the surface structure of the filament arising from the bead-spring model. The second set of simulations considers *rough filaments* with $\sigma \simeq 1$ (§4); as shown below, the corrugated filament surface resists relative tangential sliding and thus qualitatively alters the collective filament dynamics.

For all simulations, we keep the filament contour length constant: we set the number of beads $N_m = 40$ and set a large extensional spring constant $\kappa_E = 2\times 10^4 k_B T/\ell_0^2$ so that the filament is practically inextensible. Since the filament dynamics is sensitive to its bending rigidity, B, we consider three values of B, and thus three values of β (Table.2, Eq. 7). To mimic situations in which active filaments are connected by linkers (rigid or flexible) to a substrate, we usually specify that one end of the active filament is clamped rigidly at $s=0$ (except for Figs. 9 and 10, in which we allow the end of the filament attached to the wall to freely pivot). We initialize simulations with each filament in a straight configuration, for which the active forces are oriented toward the

β	$\mathscr{A}_{\max}/\ell_0$	$\omega\ell_0^2/D$
192	20	1.4×10^{-2}
384	16.5	1.75×10^{-2}
768	14	2.1×10^{-2}

Table 2 Amplitude $\mathscr{A}_{\max}$ and frequency ω of oscillations of an isolated filament for three values of the activity number, β (defined in Eq. 7).

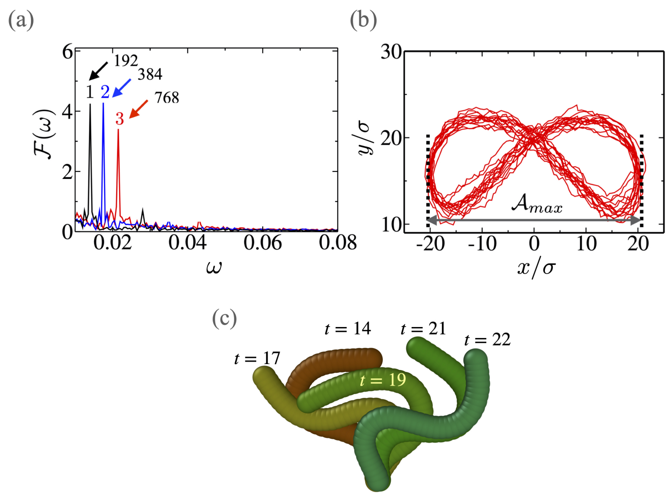

Fig. 2 (a) Fourier transform $\mathscr{F}(\omega)$ of the end-end distance L_{ee} indicating distinct frequency peaks at (1) $\beta=192$, (2) $\beta=384$, and (3) $\beta=768$. (b) The trajectory of the end-segment of a filament with $\beta=192$. $\mathscr{A}_{\max}$ denotes the maximum displacement of the end-segment along the x direction, averaged over many oscillatory cycles. Note the figure of 8 patterns due to geometric symmetries in the problem. (c)) Typical configurations of an isolated filament during an oscillatory cycle (indices represent times) for dimensionless activity strength $\beta = f(N_m-1)^3\ell_0^3/B = 384$. Note that $\ell_0=1$ in reduced (simulation) units. The roughness parameter σ is not relevant for the single filament case.

clamped base, causing a compressive stress along the filament. We emphasize however that our boundary condition confers restrictions to the filament position and conformation at $s=0$. Since hydrodynamics is ignored and we do not solve for fluid velocities, we do not simulate an actual wall.

For sufficiently large active force magnitude f, since the direction of F is aligned to the local unit vector along the arc-length of the filament and directed toward the clamped end, each filament undergoes a buckling transition and eventually nonlinear oscillations[33,35,36]. The follower force mechanism couples the filament configuration to the active force. Steric interactions between neighboring filaments significantly alter filament orientations and thereby the active-follower forces. Thus, filaments within a carpet undergo different dynamics than the intrinsic beating motions of isolated filaments.

2.4 Behavior of an isolated filament

Just as a single bead constitutes the irreducible unit element of a filament, a single chain/filament constitutes the appropriate unit element to analyze multi-filament clusters and arrays. Here we summarize our previous simulation results (finite noise) and the analytical results in the continuum, noiseless limit.

In previous investigations of a similar system[32,33], we studied the spatiotemporal stable dynamics of a single noisy filament under two conditions - clamped at $s=0$ and free at $s=L$, or pivoted at $s=0$ and free at $s=L$. In[33], we allowed the follower force direction to deviate from the tangent vector. Here, as shown in equations (1)-(6), we have removed this degree of freedom and thus the only element of stochasticity is due to thermal diffusion of the beads comprising the filament.

2.4.1 Previous results for noisy active filaments

In the case of a single *clamped filament*, the spatiotemporal response obtained from equations (1)-(6) depends solely on the dimensionless parameter β. Roughness does not play a role in this limit, as it is relevant only when multiple filaments interacting sterically. For $\beta < \beta_c$, the filament remains nearly straight with small amplitude fluctuations in the contour due to noise, with $\beta_c \approx 76.2$ (consistent with the exact value determined by a linear stability analysis in the noiseless limit $D=0$[32]). For $\beta > \beta_c$, the straight filament yields to an oscillating state. When $\beta \gg \beta_c$, interplay between active energy injected into the oscillating filament, the elasticity of the filament, and dissipation in the ambient fluid sets the frequency of oscillation and the maximum amplitude of the oscillations. Scaling arguments then provide estimates for the frequency of oscillations[33] $\omega \sim \kappa/(\eta\ell^4)\,\beta^{\frac{4}{3}}$ where η is the viscosity of the ambient fluid. Furthermore, the oscillating filament has a well-defined amplitude whose maximum value $\mathscr{A}_{\max}$ varies monotonically with β for the range of parameters we consider. Since the filament is clamped at one end, the lateral motion of the filament is maximal at the free end with the tip executing a figure-of-eight pattern, with amplitude $\sim (N_m-1)\ell_0/\beta^{\frac{1}{3}}$. The filament tip has width σ, and thus moves a distance $\sim \mathscr{A}_{\max} \equiv (N_m-1)\ell_0/\beta^{\frac{1}{3}}$. Since we ignore hydrodynamic coupling between the filaments, two filaments separated by a distance $\Delta > \mathscr{A}_{\max}$ will behave predominantly as isolated filaments. The extent of steric coupling is quantified by geometric dimensionless parameters δ and $\delta_{\max}$:

$$\delta \equiv \frac{\Delta-\sigma}{\ell_0}, \tag{8}$$

$$\delta_{\max} \equiv \frac{\mathscr{A}_{\max}-\sigma}{\ell_0} = \left[\frac{(N_m-1)}{\beta^{\frac{1}{3}}} - \frac{\sigma}{\ell_0}\right]. \tag{9}$$

For $\beta \gg 1$, we see that two filaments are closely spaced if $\delta \sim 1$ and loosely spaced when $\delta \sim \delta_{\max}$. In Figure 2(a)-(c) we present the oscillatory dynamics of a clamped filament in the limit $\delta \gg \delta_{\max}$. For sufficiently large activity ($\beta=192$) the filament undergoes regular oscillatory motion (Fig 2(a,b)), with a peak in the power spectrum at a frequency that depends on β (Figure 2(a)). Moreover, the end-segment of the filament oscillates between two maximum values, whose amplitude is denoted by $\mathscr{A}_{\max}$ Figure 2(b)). In the present work, the drag force acting on the filaments is calculated with *local Resistive Force Theory (RFT)*, and thus hydrodynamic interactions (HI) between different parts of the filament are neglected.

2.4.2 Non-local hydrodynamics in single filaments

We also computationally and theoretically analyzed an isolated active filament that is pivoted at $s = 0$. In this scenario, beyond a critical value $\beta \approx 20.19$, the filament undergoes a rotating instability[32]. Simulations with local RFT drag as well as non-local hydrodynamics yield filament dynamics that are qualitatively similar[33].

We have also previously studied the effects of anisotropic bead mobility and long-ranged, non-local hydrodynamic interactions between filament segments (see ESM Appendix C[33]. There, we used a hybrid simulation technique in which molecular dynamics simulations for the filament were combined with a mesoscale hydrodynamic simulation method, multi- particle collision dynamics (MPC), for the ambient fluidic environment. We found that including non-local hydrodynamic interactions for the driven active filament leads to slightly smaller lateral amplitudes and increases the beating frequency. Beating patterns with hydrodynamics interactions are qualitatively similar to non-hydrodynamic simulation results. The frequency scaling with active force density, and the critical active force required for oscillations are the same in both cases. Such qualitative similarities in oscillations are reported in similar analytical models as well[34]. The results for critical onset of oscillations and the emergent frequency compare well with the exact calculations with full hydrodynamics[36,37]. The latter calculation also include a no-slip rigid wall to which the filament is grafted[36,37].

3 Small clusters of smooth filaments

An array with $N \gg 1$ filaments may be understood as a hierarchical network, comprising of filament pairs, filament triplets, and so on. Therefore, to understand the emergence of synchronization at small scales, we first study a two-filament pair and a three-filament bundle to identify coordination and synchronization at small scales, followed by a large carpet ($N = 300$) to learn how these behaviors extend to larger scales. Except where mentioned otherwise we consider smooth filaments with $\sigma = 4\ell_0$.

3.1 Two-filament pairs

We first consider two filaments with bases that are clamped and separated by a distance Δ along the x axis. The clamped boundary implies that both the position and the angle at the end $s = 0$ are fixed. The available space between two active filaments is then given by $\delta = (\Delta - \sigma)/\ell_0$. Since the isolated filament dynamics is governed by the activity number β, we compare the oscillatory dynamics of the filaments for three values, $\beta = 768$, 384, and 192. Based on the simulation results, we observe three different class of oscillations, depending on the values of δ and $\mathscr{A}_{\max}$. For for $1 < \delta \ll \delta_{\max}$ both filaments oscillate synchronously. However, the synchronized oscillations are disrupted at higher separation, $1 \ll \delta < \delta_{\max}$. Interestingly, synchronization re-emerges when δ is increased further, $\delta \simeq \delta_{\max}$. The details of this analysis are explained in SI§I and Fig.S1.

3.2 Three-filament clusters

We next study a group of three filaments ($N = 3$), with each separated by δ at the base. This arrangement breaks the symmetry of the constituent filaments, since the central filament experiences steric hindrance on both sides while the end filaments each have a neighbor only on one side. Similar to the analysis for two-filaments, we study the system for three values of β, as a function of the basal separation δ.

3.2.1 Tightly packed filaments ($\delta \simeq 1$): synchronization

All filaments interact strongly at $\delta \simeq 1$. Computing the L_{ee} waveform and the end-point trajectory of each filament shows that the waveform is similar for both the end-filaments while it differs for the middle filament (in both amplitude and frequency, Fig 3(a)). The maximum amplitude of $L_{\mathrm{ee}}(t)$ attained by the middle filament is roughly half that of the end-filaments and the associated frequency is almost double. The reason for this difference is evident from the end segment trajectories (Fig. 3(b)), which show that the oscillation of the middle filament is occluded by the steric hindrance due to both end-filaments. This leads to a low-amplitude, symmetric pattern for the middle filament. For the end-filaments, the oscillations are obstructed only in one direction, which leads to asymmetric patterns. This asymmetry manifests as an additional low-frequency mode in the L_{ee} waveform.

3.2.2 Intermediate packing ($1 < \delta < \delta_{\max}$): disruption and trapping

At intermediate spacing, the filaments have space to deform without contact, and we observe a disruption of regular oscillations for all three filaments. Since the deformation depends on the filament softness ($\sim 1/\beta$), it is especially pronounced for soft filaments with $\beta = 768$, where the oscillatory pattern is highly sensitive to δ at this range as highlighted in Fig 3(c)-(h).

At $\delta = 7$, the $L_{\mathrm{ee}}(t)$ time series shown in Fig. 3(c) shows neither regular oscillations nor synchronization, and the end-segment trajectory does not exhibit a clear pattern (Fig. 3(b)), especially for the middle filament.

We observe a similar trend in the dx/dt vs x pattern at this spacing (SI§1-B). The regular oscillation is recovered when $\delta = 10$, while the end-point trajectories of all three filaments are asymmetric but similar (Fig 3(f)). However, for $\delta = 12$ (Fig 3(h)), the end-segment trajectory of the middle filament is qualitatively different compared to the end filaments. While the end-filament oscillation switches from symmetric to asymmetric patterns and back, the centre filament always oscillates asymmetrically. The direction of this asymmetry switches over time, thus resulting in an overall symmetric, butterfly-like pattern over a large time (Fig 3(g-h)).

However for stiffer filaments with $\beta = 384$ and 192 (SI§1-B), we do not observe such a disruption in oscillations as for soft filaments. In this case, the middle filament is trapped either below or the end filaments, restricting its oscillatory amplitude without disrupting the regular oscillations. When the separation is further increased to $\delta \simeq \delta_{\max}$, the filaments do not interact except for the maximally bent (minimum L_{ee}) configurations. At this separation, we observe a reemergence of synchronized oscillations in all the filaments for all values of β (SI§1-C).

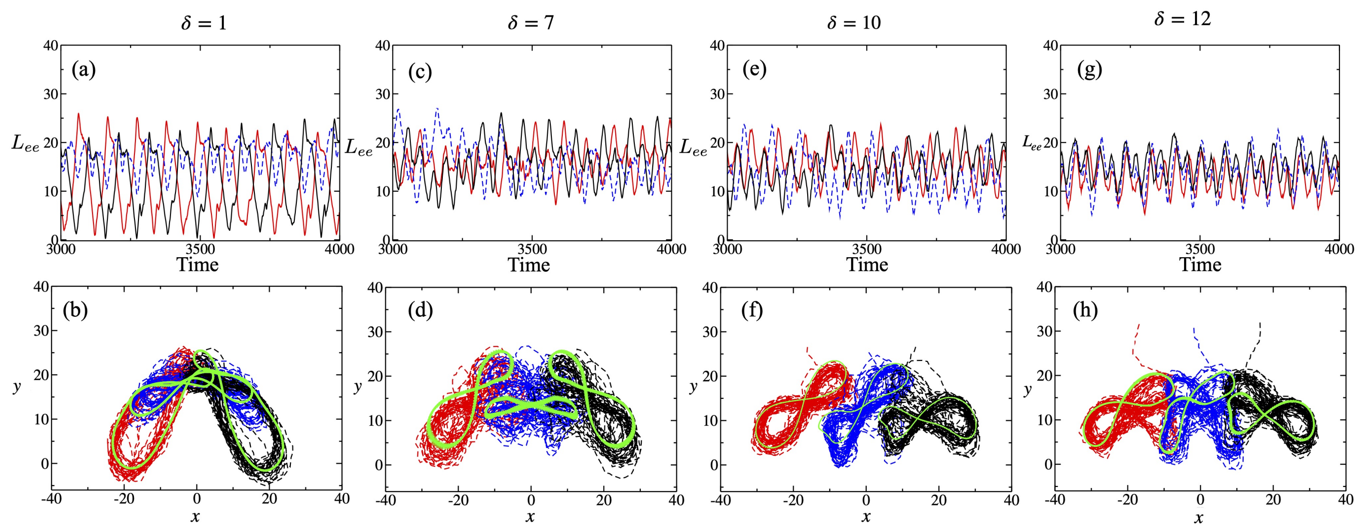

Fig. 3 Dynamics of three clamped filaments. The time evolution of the end-end length $L_{\rm ee}$ and the end-segment trajectory are shown for inter-filament separations $\delta = 1$ ((a) & (b)), $\delta = 7$ ((c) & (d)), $\delta = 10$ ((e) & (f)), and $\delta = 12$ ((g) & (h)). All the filaments have activity number $\beta = 768$ so that $\delta_{\rm max} = 10$. The green curves in the second row correspond to the trajectories when noise is negligible. We note that the discreteness of the simulation scheme results in the green curves not being completely smooth. We also note the similarities in (f) and (h), with a more pronounced asymmetry toward one of the end filaments for $\delta = 12$.

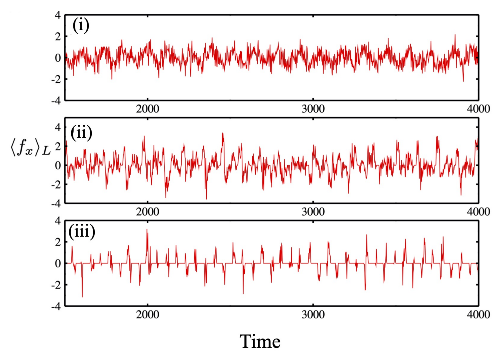

Fig. 4 The x component of the mean contact force that acts on the middle filament in a three-filament cluster. (a) Here $\beta = 384$ (i) $\delta = 1$, (ii) $\delta = 8$ and (iii) $\delta = 17$ (δmax $\simeq 16.5$). Plots for $\beta = 192$ are qualitatively similar.

3.3 Going from $N \sim O(1)$ to $N \gg 1$: Anticipating the effect of contact forces

To anticipate how this time-dependent nature of the steric interactions will effect the collective behavior of $N \gg 1$ filaments, we measure the components f_x and f_y and magnitude $|f|$ of the *contact* forces,

$$\langle f_x \rangle = \frac{1}{N_{\rm m}} \sum_{\alpha=1}^{N_{\rm m}} (\mathbf{F}_\alpha^{Ex} \cdot \mathbf{e}_x), \quad \langle f_y \rangle = \frac{1}{N_{\rm m}} \sum_{\alpha=1}^{N_{\rm m}} (\mathbf{F}_\alpha^{Ex} \cdot \mathbf{e}_y) \tag{10}$$

derived from the pairwise WCA potential, acting on the middle filament as a function of time for the soft filament with $\beta = 384$ (Fig. 4). For small basal separation ($\delta = 1$), the middle filament is always in contact with the neighboring filaments and $\langle f_x \rangle$ exhibits regular, albeit noisy, oscillations (Fig. 4(i)). When the basal distance is increased $\delta \simeq 10$, the periodicity in $\langle f_x \rangle$ weakens and the pattern is more noisy (Fig 4(ii)), which is consistent with the observed destruction of regular oscillations. At large basal distances ($\delta \simeq 17$) the filament interacts with its neighbors only for a short time during the oscillation cycle, which manifests as regular pulses in $\langle f_x \rangle$ pattern (Fig 4 (iii)). Such periodic pulses lead to a highly synchronized response over this range of distances.

4 Periodic array of smooth filaments

We now consider a larger system with $N = 300$ filaments arranged on a one-dimensional lattice. As above, we consider smooth filaments with uniform spacing δ. We apply periodic boundary conditions in the x direction such that the periodic images of the end filaments (1st and 300th) are also separated by δ, so that in the absence of spontaneous symmetry breaking, all filaments are identical. We choose an intermediate filament rigidity value, with $\beta = 384$.

4.1 Tightly packed filaments ($\delta \simeq 1$): Slow metachronal waves

Under tight packing, steric interactions act on each filament throughout its oscillation cycle, which leads to a high degree of inter-filament coordination (Fig 5 (a)) (see MOVIE-1 in ESM). As in the small clusters studied above, we quantify the spatiotemporal behavior of the system via the end-end length $L_{\rm ee}$ of each filament as a function of time. We plot this information in a kymograph in Fig.5 (b), where the spatial points are the basal position of each filaments. The color code indicates $L_{\rm ee}$ of each filament with basal anchoring at x. The kymograph (Fig 5 (b)) indicates a phase-lag synchronization in beating between filaments separated by large distances. This manifests as metachronal waves, propagating in a specific $(+x)$ direction, similar to the traveling waves observed in many biological systems. Due to the high inter-filament coordination, waveforms of each filament are similar (Fig 5 (c)).

However, the waveform and amplitude of $L_{\rm ee}$ are significantly

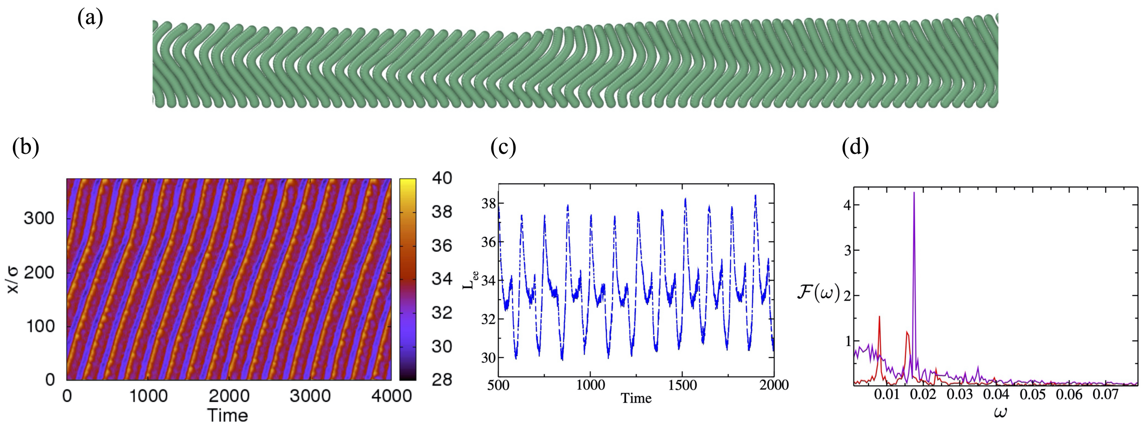

Fig. 5 Collective dynamics of clamped filaments. (a) Snapshot of a section of $N = 300$ closely packed ($\delta = 1$) clamped filaments undergoing synchronized beating at $\beta = 384$. Videos of corresponding simulation trajectories are shown in MOVIE-1 in the ESM. (b) Kymograph of the end-end distance L_{ee} of clamped filaments for $\delta = 1$. The color code indicates the end-end length L_{ee}. The 0 on the y-axis corresponds to the left end of the filament array. The slanted line indicates propagation of a stable waves in the $+x$ direction. (c) Typical oscillatory pattern of individual filaments for $\delta = 1$. The filament-filament interaction significantly reduces the filament oscillatory amplitude and frequency compared to isolated filaments. (d) Comparison of the oscillatory frequency of an individual filament inside the carpet, quantified via the Fourier transform of the end-end distance (L_{ee}) time-series, for the tightly packed condition $\delta = 1$ (red) and for isolated filaments with no inter-filament interactions $\delta \gg \delta_{max}$ (purple), at $\beta = 384$.

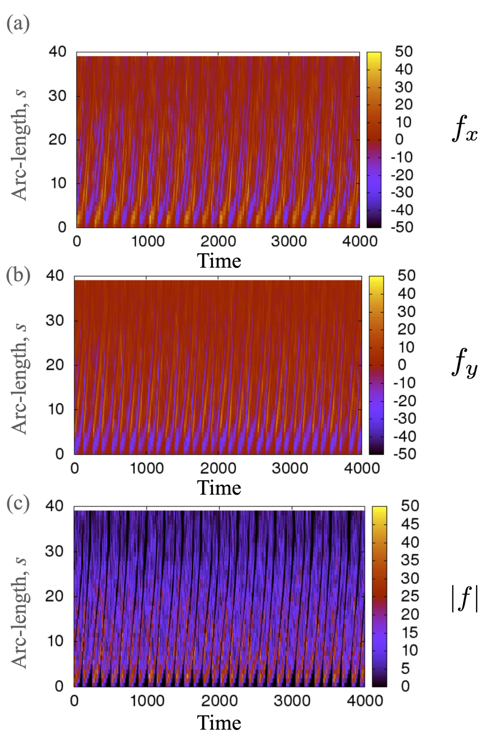

Fig. 6 Kymographs of force components due to inter-filament repulsive interactions on sections of a filament, in a dense array of $N = 300$ smooth filaments with $\delta = 1$. (a) The x component, (b) y component, and (c) magnitude $|f|$.

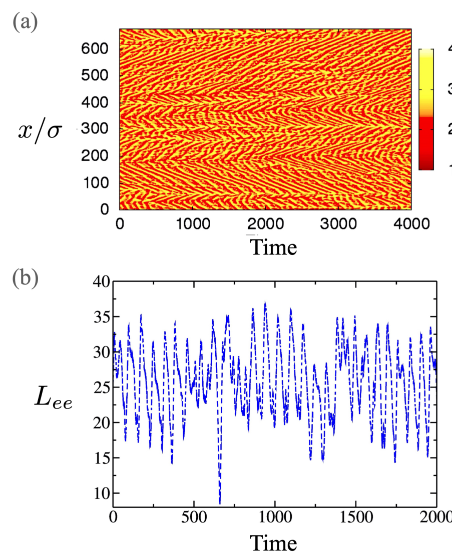

Fig. 7 (a) Kymograph of the end-end length L_{ee} in system of $N = 300$ clamped filaments for the spacing parameter $\delta = 5$ with $\beta = 384$. Videos of corresponding simulation trajectories are shown in MOVIE-2 in the ESM. The 0 on the y-axis corresponds to the left end of the filament array. The disordered pattern in the kymograph indicates a lack of synchronization in filament oscillations. (b) Typical waveform of L_{ee} of an individual filament from the same arrangement, indicating the disorder in oscillations.

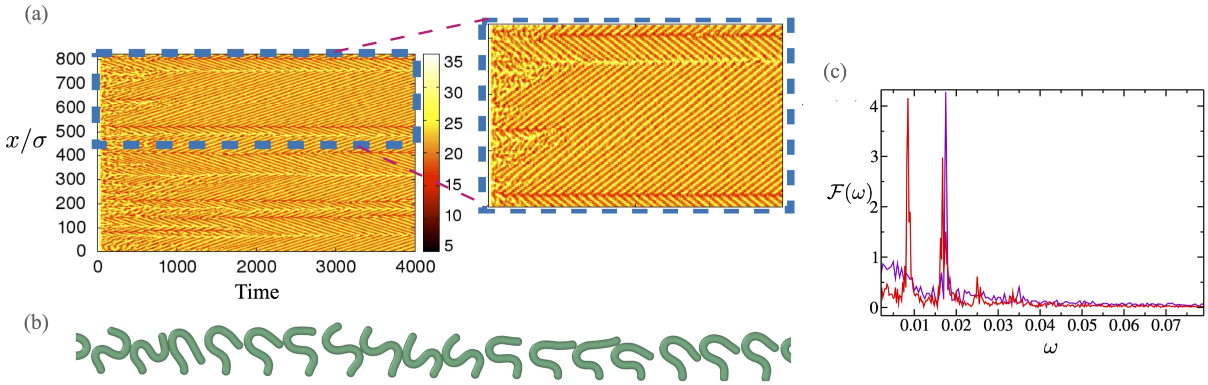

Fig. 8 Collective dynamics of sparsely packed filaments. (a) Kymograph of the end-end length $L_{\rm ee}$ in a system of $N = 300$ clamped filaments for the spacing parameter $\delta = 11$ with $\beta = 384$. Videos of corresponding simulation trajectories are shown in MOVIE-3 in the ESM. The 0 on the y-axis corresponds to the left end of the filament array. The thin, slanted patterns correspond to fast-moving waves translating in both the directions. A blown-up version of the kymograph is shown on the right. (b) Snapshot of a section of filament array, indicating a phase-lag synchronization. (c) Individual filament oscillation frequencies in a sparsely packed carpet $\delta = 11$ (red) and for isolated filaments $\delta \gg \delta_{\rm max}$.

different from those of an isolated filament. Fig 5(d) compares the Fourier transforms of the $L_{\rm ee}$ time-series for isolated filaments and those within the carpet, demonstrating that the steric interactions significantly reduce the oscillation frequency.

Since our results indicate that steric interaction between the filaments plays a crucial role in the emergence of cooperative oscillations, we analyze the dynamics of inter-filament forces acting on a filament due to inter-filament interactions. Fig. 6 shows kymographs of the components and magnitude of the steric forces. Since the oscillatory motion alters the local 'contact' of a filament in the array, the contact forces also exhibit spatiotemporal dynamics similar to Fig. 5(b). The striped pattern in Fig 6 indicates a contact propagation from the basal to the distal end of the filament. However, the periodicity in the pattern is almost double for the F_y component compared to the F_x component, which is specific to the filament oscillatory dynamics.

4.2 Intermediate separation: Irregular beating

Increasing the inter-filament spacing leads to disordered filament dynamics (Fig. 7 (a) and ESM MOVIE-2); the kymograph shows a lack of phase-lag synchronization or coordinated oscillations of spatially separated filaments. The lack of coordination results from irregularities in the beating patterns of individual filaments induced by interactions with their neighbors (Fig 7 (b)). Thus, the disappearance of coordinated beating at intermediate filament separations described above for $N = 3$ extends to large systems with $N \gg 1$.

4.3 Large separation: Emergence of fast metachronal waves

When the inter-filament spacing is further increased ($\delta > \delta_{\rm max}/2$), the contact interaction becomes 'pulse'-like and the individual filaments beat with a higher frequency, close to that of an isolated filament. Interestingly, we observe the reemergence of waves at these large separations (Fig 8 and ESM MOVIE-2). However, the wave propagation is qualitatively different than observed for tightly packed filaments, where filaments are in continuous contact with their neighbors. At large separations, the filaments which are initially oscillating independently, coordinate their oscillatory phase through the 'pulse'-like interactions. This results in nucleation of independent waves moving in either directions, at different regions in the array of filaments. Two oppositely moving waves meet at a 'node' where they annihilate (c.f Fig 8 (a)), leading to a saw-tooth pattern in the kymograph. Also, the speed of wave propagation, which is closely linked to the individual filament beating frequency, is higher compared to the tightly packed filaments.

A closer examination of the configuration (Fig 8 (b) and MOVIE-3) indicates that the filaments exhibit a phase-lagged synchronization, with a much larger phase difference compared to $\delta \simeq 1$. Analysis of the frequency spectrum of $L_{\rm ee}$ oscillations identifies multiple harmonics in the oscillation waveform (Fig. 8(c)). However, the oscillation frequency of individual filaments at this separation closely matches with that of an isolated filament (Fig. 8(c)).

5 Periodic array of rough filaments

The previous section discusses the collective dynamics of active filaments for which the individual beads have an effective interaction diameter $\sigma = 4\ell_0$ that is larger than the equilibrium separation between neighboring beads ℓ_0. This arrangement ensures relatively low resistance to tangential sliding between adjacent filaments in tightly packed configurations and mimics steric interactions between brush-grafted filaments as in the mucociliary tract[56]. In this section, we discuss filaments in which the effective interaction diameter is comparable to the equilibrium inter-bead distance ($\sigma \approx \ell_0$), resulting in large gradients of the excluded-volume potential between adjacent filaments and mimicking filaments with corrugated micro-scale roughness[57–59]. Effectively, beads in neighboring filaments interlock as they move, resulting in higher effective friction coefficients and significantly reducing their tangential velocities.

Additionally, we explore the role of the geometric constraint at the base in sustaining and stabilizing oscillations. Surprisingly, relaxing the hard clamped boundary condition by the softer pivot-

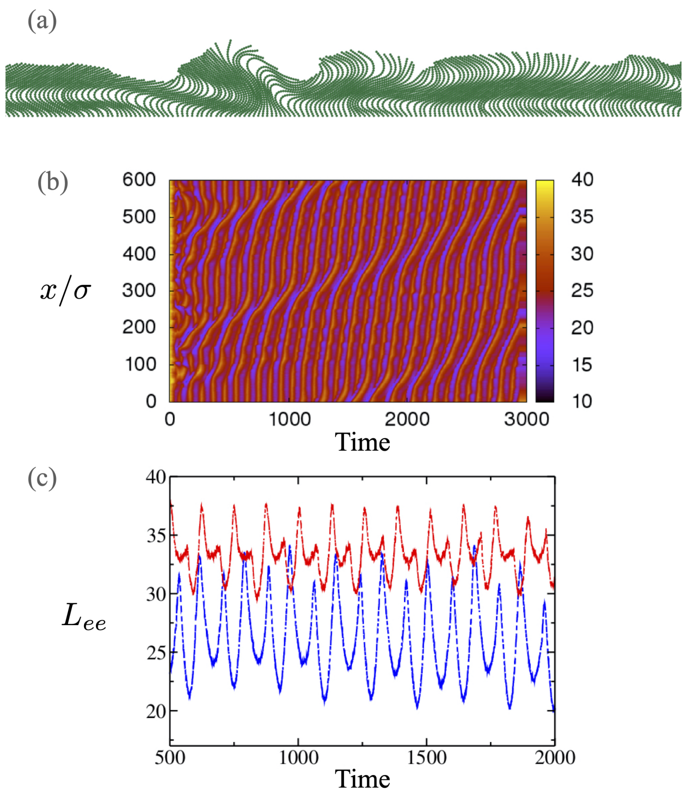

Fig. 9 Collective dynamics of *rough* filaments ($\sigma/\ell_0 = 1$), with $\beta = 384$ and clamped at the base. (a) Typical configuration for tight packing ($\delta = 1$), exhibiting regions with synchronized oscillations. (b) Kymograph of the end-end distances of the filaments. Vertically aligned stripes indicate synchronized oscillations. (c) Typical oscillatory pattern of an individual, rough filament at $\delta = 1$ (red). The oscillatory pattern qualitatively differs from that observed for smooth filaments with $\sigma/\ell_0 = 4$ (blue).

type condition that allows for rotation leads to a new pattern - stable actively jammed structures.

5.1 Rough filaments with clamped bases

Fig 9 and (ESM-MOVIE-4) present the collective dynamics of $N = 300$ clamped active rough filaments. To highlight the effect of inter-filament interactions, we focus on tight packing with $\delta = 1$. The activity parameter is $\beta = 384$. As in the case of smooth filaments, excluded volume interactions alter the phase of oscillation of individual filaments (in the array), leading to collective oscillatory patterns (Fig 9(a)). However, the patterns qualitatively differ from those exhibited by smooth filaments at $\delta = 1$ (Fig. 5(b)). Instead of forming long-ranged metachronal waves that travel across the entire array, the interlocking of neighboring rough filaments results in clusters of synchronously oscillating filaments with negligible phase differences among filaments within a cluster. These clusters are separated by smaller regions of filaments that oscillate with a constant phase shift, forming short-ranged metachronal waves.

The kymograph in Fig 9(b) illustrates this behavior, and indicates a complex collective dynamics of the filaments. The vertical stripes in the kymograph indicate groups of filaments with synchronized oscillations, while the curved regions in the stripes correspond to shifting in the location of synchronized clusters along the array. Fig. 9(c) shows the typical oscillatory pattern of individual filaments via their end-end length, $L_{\rm ee}$, which reveals the modification in oscillatory pattern of individual filaments due to crowding.

5.2 Rough filaments with a pivoted bases

We now consider filaments with a pivoted boundary condition at their bases, meaning rotation about the anchoring point is not energetically penalized. Our previous work showed that individual filaments with pivoted boundary conditions undergo rotational motion with a constant frequency (see [32,33,43]). Here, we examine how inter-filament interactions change this behavior by simulating an array of such filaments at $\delta = 1$ ($N = 300$) and $\delta = 0.3$ ($N = 600$) keeping the domain size the same. As before periodic boundary conditions are applied to the lateral ends. Note that since we do not account for excluded volume interactions between the filaments and anchoring surface in our simulations, and filaments are either clamped or pivoted at the point $s = 0$, the pivoted boundary condition would enable smooth filaments to slide past each other and point downward. However, for rough filaments, sliding is sufficiently restricted at small separations that this inversion does not occur. We therefore focus on rough filaments in the following.

Figures 10 (a-c) and ESM Movie 5 provide a mechanistic picture of the dramatic changes in collective spatiotemporal patterns triggered by softening the boundary conditions at the base from a hard (clamped) condition to a less restrictive pinned condition. Considering the results shown in Figs 10(a,b) with ESM-Movie5, we make the following observations. Relaxing the boundary condition quenches the traveling metachronal waves and wavetrains seen previously; instead, we observe periodically spaced jammed, static clusters (bundles) of filaments. Moving between these jammed bundles and reflecting off them are un-jammed filaments that oscillate. Since the net force inside a static structure must be zero, each jammed cluster has a nearly symmetric shape; furthermore, the distance between the static clusters depend on both geometric properties of the array (filament length L and spacing parameter δ, as well as the activity β). For fixed activity and length L, decreasing δ results in closer, thicker, and lower aspect ratio bundles (c.f Fig. 10(a) vs. 10(b)).

Focusing more on the intermediate $\delta = 1$, case we plot in Fig 10(c), (i) and (ii) the force distributions in the bundles, (iii) the kymograph of the filament end-end length dynamics, and (iii) the trace of the free end of a representative oscillating filament (dashed blue line) compared with a static filament inside the bundle (red). We examine and interpret each of these figures in more detail below.

To understand the mechanism that drives rough filaments with pivoted boundary conditions to form jammed clusters, we analyze the inter-filament forces within jammed clusters. Fig 10(a,b) maps the net magnitude of the excluded-volume force ($|F^{\rm Ex}|$, eq. 5) on each bead within the clustered configurations - here Fig. 10(a) illustrates the force map for $\delta = 1$. The map indicates that the interaction force is largest near the middle of the jammed cluster, where cluster undergoes maximum compression

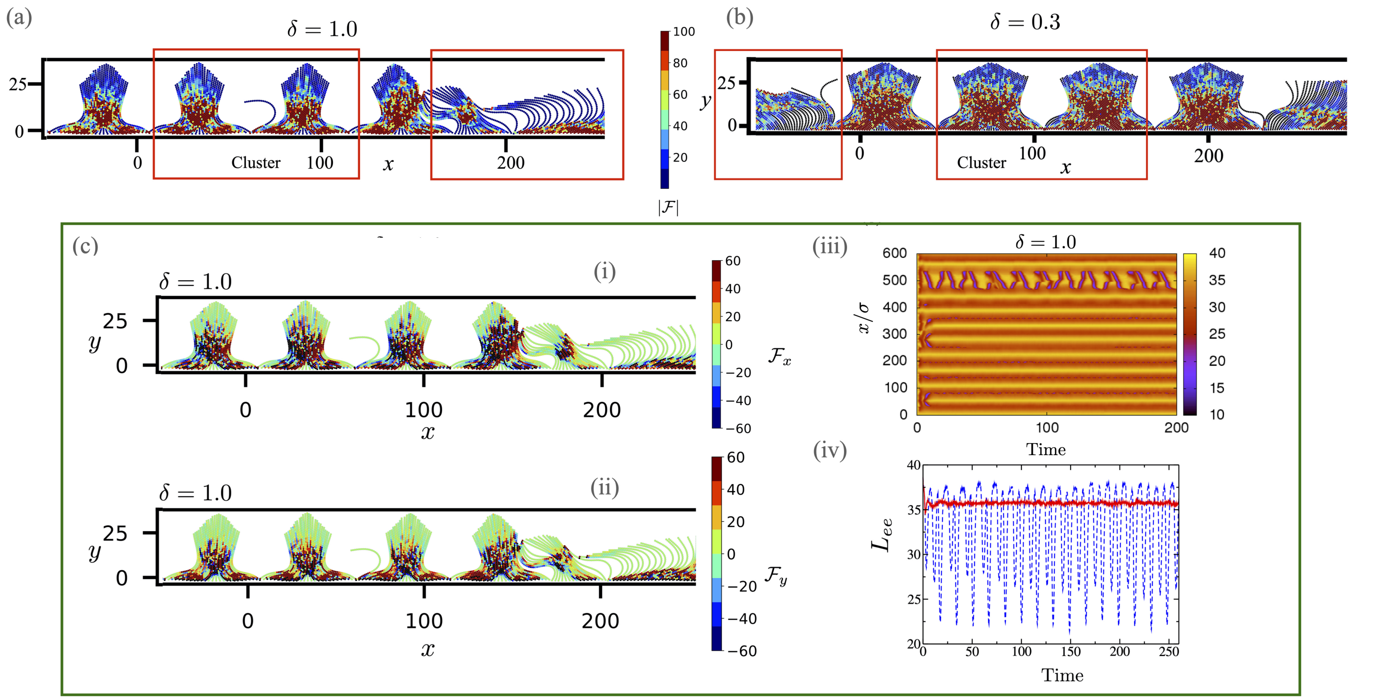

Fig. 10 Collective dynamics of *rough* filaments with *pivoted* boundary conditions at the filament bases. Typical configuration for packing densities, (a)$\delta = 1.0$ with $N = 300$ filaments, and (b) $\delta = 0.3$ with $N = 600$ filaments. Periodic boundary conditions are applied at the lateral boundaries, so the first and the 300th (for $\delta = 1.0$) or the 600th (for $\delta = 0.3$) filament are neighbors. In both cases the filaments form jammed, static clusters, interspersed among groups of oscillating filaments. Here the colour maps indicate magnitude of total contact forces ($\mathscr{F}$) on each monomer measured from the WCA interaction potential, for a configuration with pivoted boundary conditions with $\beta = 384$. (c) (i) The x component and, (ii) the y component of the total contact forces on each bead for the configuration with $\delta = 1$. Note that we show most but not all of the array. (iii) Kymograph of the end-end distance of the filaments for the $\delta = 1.0$ case. Horizontal stripes indicate the static clusters. (iv) End-end length of a dynamic filament with $\delta = 1$, which oscillates between two static clusters (blue) and a static filament (red).

due to the active forces.

In addition to the total force, the symmetric internal force distribution is evident upon examination in Figs 10(c)(i)&(ii), of individual x and y components of the forces respectively. We observe that the x component of the contact force is marginally higher compared to the y component, as the compression due to the outer filament acts mainly along the x direction. This is reminiscent of stresses borne by an arch - the distribution of compressive forces suggests that filaments can relax and unravel only by further compression given the direction of the active force thus vertically stabilizing the cluster. Lateral stabilization comes from the momentum impulses imparted to a cluster along the x-direction as unjammed oscillating filaments fit against the edge. Finally, there is also a geometric component due to the connected bead filament. Closer examination of the arrangement of active beads within the jammed cluster shows a nearly hexagonal packed structure that also resists sliding of beads strongly. Both these are signatures of roughness playing a dominant role. We note also that low to moderate noise can cause co-moving sterically interacting filaments to further align as we found in dense nematic suspensions [60]. This increased tendency to align combined with the increased bending stiffness of the bundled cluster stabilizes it from collapsing.

Moving next to the kymograph in Fig.10(c)-(iii), we observe yellow horizontal stripes corresponding to static clusters and slanted patterns corresponding to the small regions of oscillating filaments in between static clusters. Note that not al filaments moving between adjacent bundles behave similarly - filaments may move and then get stuck, keep periodically orscillaing and sometimes dislodge jammed filaments from the bundles. Fig 10(c) (blue dashed line) shows the typical oscillatory pattern of the un-jammed filaments, which is similar to that of filaments with clamped boundary conditions at roughly similar δ ($\delta = 1.3$ for the pivoting case and $\delta = 1$ for the clamped case). In Fig 10(c)-(iv), the red solid line emphasizes that filaments trapped inside the bundle (well into the interior) are almost non-moving. The end-end length $L_{\rm ee}$ is invariant in time for such filaments and roughly equal to the filament length.

Beyond $\delta = 2.0$, we find that the clusters are very sparse since the filaments have more space in between and can rotate past each other. This response is an artefact caused due to the lack of an actual physical barrier preventing filaments from completely sliding and moving around the pivot.

6 Summary and Perspectives

6.1 Summary

We have shown that purely short-ranged contact interactions are sufficient to drive coordinated beating among large arrays of active filaments, in which individual filaments beat due to compressive elastic instabilities. Moreover, such filament arrays exhibit a rich panoply of emergent behaviors, depending on the inter-filament spacing, the many-body nature of the filament-filament interaction, and how filaments are attached to a surface.

Of particular interest, large arrays of smooth, tightly packed filaments exhibit highly coordinated oscillations that manifest as propagating metachronal waves. Coordination and hence metachronal waves diminish as the inter-filament spacing increases, but then reemerge at large inter-filament separations on the order of (but less than) the oscillation amplitude. Notably, the form of the metachronal waves is qualitatively different at small and large inter-filament spacing.

To understand the origin of the spatiotemporal patterns and stable states, we have systematically studied the dynamics of small clusters containing two or three filaments in addition to the large arrays. In the small tightly packed clusters of smooth filaments, coordination results in highly synchronized oscillations. Analogous to the large arrays, synchronization decreases with increasing inter-filament spacing but then reemerges at spacing comparable to the oscillation amplitude. The form of the metachronal waves in large arrays can be understood from the changes in amplitude and waveform exhibited by the small clusters at different spacing.

We also find that the nature of spatiotemporal patterns and type of stable state qualitatively differ depending on whether the filament-filament interaction is smooth or rough (corrugated) and how the filament is attached at its base. Rough filaments interlock with their neighbors at tight packing, which inhibits filament sliding motions. For rough filaments that are clamped at their base, this results in finite-size highly synchronized clusters, separated by regions of filaments undergoing asynchronous meeting. In contrast, rough filaments that freely pivot at their base form finite size *static* clusters with a size and shape that depends on the control parameters.

6.2 Future extensions

Three possible avenues for further work are evident. First, our results provide the foundation to study spatiotemporal patterns in active filament systems with full hydrodynamic interactions, particularly for colloidal active filaments such as chains comprised of self-propelling, polar particles, or a bed of colloidal chains immersed in an active fluid such as a bacterial suspension. In the case of a single filament, previous work using multi-particle collision (MPC) algorithms (Appendix in[33]) suggests that hydrodynamic interactions play a minor role, as the extra viscous friction in a 2D system for relative motions between filament segments has a logarithmic dependence on separation. For very small gaps these interactions are subdominant compared to the excluded volume constraint. Further, results in the noise-less limit[37] suggest that for a single active filament clamped to a no-slip flat surface, hydrodynamic interactions quantitatively, but not qualitatively, change the onset of oscillations, frequencies and amplitudes.

However, for multiple filaments hydrodynamic interactions are anticipated play an important role in triggering and sustaining elastic instabilities, as predicted for noise-less smooth active filament clusters and arrays with full hydrodynamics interactions, but in the absence of steric interactions[36–39]. Sangini et al. [37] suggests the existence of two unstable modes, in which the filaments respectively beat in-phase or anti-phase. Combining the results from Sangini et al. [37] with our analysis here, we hypothesize that hydrodynamic interactions and steric interactions offer two alternate mechanisms to stable states. Phase variations that lead to wavetrains or metachronal waves are expected to be affected by both physical mechanisms; with the relative importance determined by the physical system. For example, hydrodynamic interactions may dominate in biological settings, while steric interactions may need to be considered in the context of active colloidal chains.

Second, our results suggest a route to understanding synchronization and collective behavior using reduced dimensional models. Current studies, focused on interactions between rotating colloids using extensions of the Kuramoto theory[45,46], can perhaps be extended to studies of synchronization between arrays of oscillating elastic filaments. The numerical results presented here demonstrate that propagation of metachronal waves in filament arrays can arise purely via short-ranged contact interactions. While the present study is limited to a specific model for the self-regulated beating dynamics of the constituent filaments, most mechanisms that generate stable, self-regulated beating motions require coupling between the internal active force and the filament. Thus, the scope of our prediction extends beyond the particular mechanism (follower force) studied here, and can be tested in other classes of models or biomimetic systems.

Finally, our computational model can be combined with advanced numerical techniques combining MPC with high-resolution Galerkin methods to analyze viscoelastic interactions between small filament clusters. These extensions will allow us to study the transport and capture of small particles by filamentous sticky beds[61], or investigate the role of viscoelasticity[62] in mediating inter-filament interactions in addition to steric effects explored in this paper. Viscoelastic effects introduce fluid relaxation time scales and also a means to temporarily store energy. Such simulations would be interesting, and especially guide the design and understanding of biomimetic active multi-filament systems immersed in non-Newtonian fluids and open new modalities of particle transport and flow control.

Acknowledgements

RC acknowledges support from SERB, India via grants SB/S2/RJN-051/2015 and SERB/F/10192/2017-2018 and computational support from the SpaceTime2 HPC facility at IIT Bombay. AG acknowledges support from the UC Senate core grant (2018-2019). MFH acknowledges support from the Brandeis Center for Bioinspired Soft Materials, via grants NSF MRSEC (DMR-1420382 and DMR-2011846), NSF DMR-1855914, NSF XSEDE computing resources (Stampede) and the Brandeis HPCC.

Competing interests

The authors declare no competing interests.

Author Contributions

RC, AG, and MH together conceived the study. RC and AG designed the computational model, performed the simulations and analyzed the results. All authors contributed to the writing of the manuscript.

Data availability

Correspondence should be addressed to RC and AG.

References

1 K.E. Machin (1963) The control and synchronization of flagellar movement, Proc. Roy. Soc. B., 158(970), 88-104.

2 C. J. Brokaw (1975) Molecular mechanism for oscillation in flagella and muscle, Proc. Natl. Acad. Sci. USA, 72(8): 3102-3106.

3 E. H. Harris, (1989) *The Chlamydomonas source book*, Academic Press, San Deigo.

4 G. B. Witman, *Introduction to cilia and flagella in ciliary and flagellar membranes* (ed. R. A. Bloodgood), Plenum, New York, pp 1-30 (1990).

5 C. Ainsworth (2007) Cilia: Tails of the unexpected. Nature 448, 638.

6 D. M. Woolley (2007) A novel motility pattern in quail spermatozoa with implications for the mechanism of flagellar beating, Biol. Cell, 99(12), 663-675.

7 B. Qin, A. Gopinath, J. Yang, J. P. Gollub and P. E. Arratia (2015) Flagellar kinematics and swimming of algal cells in viscoelastic fluids, Scientific Reports 5.

8 C. J. Brokaw (1988) Bending-wave propagation by microtubules and flagella, Math. Bioscience, 90, 247-263.

9 C. B. Lindemann, L. J. Macauley, K. A. Lesich, (2005) The counterbend phenomenon in dynein-disabled rat sperm flagella and what it reveals about the interdoublet elasticity, Biophys. J., 89(2):1165-1174.

10 C. J. Brokaw C J (2009) Thinking about flagellar oscillation, Cell Motil. Cytoskeleton. 66, 425.

11 H. Sui and K.H. Downing (2006) Molecular architecture of axonemal microtubule doublets revealed by cryo-electron tomography, Nature, 442, 475-478.

12 D. Nicastro, C. Schwartz, J. Pierson, R. Gaudette, M. E. Porter and J. R. McIntosh (2006) The molecular architecture of axonemes revealed by cryoelectron tomography, Science, 313, 944-948.

13 I. H. Riedel-Kruse, A. Hilfinger, J. Howard and F. Jülicher (2007) How molecular motors shape the flagellar beat, HFSP J. 1 192.

14 C. B. Lindemann and K. A. Lesich (2010) Flagellar and ciliary beating: the proven and the possible, J. Cell Sci. 123 519–28

15 P. V. Bayly and K. S. Wilson K S (2014) Equations of interdoublet separation during flagella motion reveal mechanisms of wave propagation and instability, Biophys. J. 107 1756.

16 P. V. Bayly and S. K. Dutcher (2016) Steady dynein forces induce flutter instability and propagating waves in mathematical models of flagella, J. Royal Soc. Interface 13, 20160523.

17 D. R. Brumley , K. Y. Wan , M. Polin, R. E. Goldstein (2014) Flagellar synchronization through direct hydrodynamic interactions, eLife 2014;3:e02750.

18 N. Pellicciotta, E. Hamilton, J. Kotar, M. Faucourt, N. Delgehyr, N. Spassky, and P. Cicuta (2020) Entrainment of mammalian motile cilia in the brain with hydrodynamic forces, PNAS 117(15), 8315.

19 T. Sanchez, D. Welch, D. Nicastro, Z. Dogic (2011) Cilia-like beating of active microtubule bundles, Science, 333(6041): 456-459.

20 T. Sanchez, D. T. N. Chen, S. J. DeCamp, M. Heymann, Z. Dogic (2012) Spontaneous motion in hierarchically assembled active matter, Nature, 491(7424): 431-434.

21 A. Ward, F. Hilitski, W. Schwenger, D. Welch, A. W. C. Lau, V. Vitelli, L. Mahadevan and Z. Dogic (2015) Solid friction between soft filaments, Nat. Mater., 14, 583-588.

22 R. Dreyfus, J. Baudry, J., M. L. Roper, M. Fermigier, H. A. Stone and J. Bibette (2005) Microscopic artificial swimmers, Nature 437(7060), 862-865.

23 Y. Sasaki, Y. Takikawa, V. S. R. Jampani, H. Hoshikawa, T. Seto, C. Bahr, S. Herminghaus, Y. Hidaka and H. Orihara (2014) Colloidal caterpillars for cargo transportation, Soft matter 10(44), 8813-8820.

24 A. E. Patteson, A. Gopinath and P. E. Arratia (2016) Active colloids in complex fluids, Current Opinion in Colloid & Interface Science 21, 86-96.

25 B. Dai, B. et al. (2016) Programmable artificial phototactic microswimmer, Nature Nanotech., 11, 1087–1092.

26 D. Nishiguchi, J. Iwasawa, H.-R. Jiang and M. Sano (2018) Flagellar dynamics of chains of active Janus particles fueled by an AC electric field, New J. Physics 20, 015002.

27 Z. Lin et. al., (2017) Light-Activated Active Colloid Ribbons, Angewandte Chemie 129, 13702–13705.

28 Y. Hong, N. M. K. Blackman, N. D. Kopp, A. Sen, and D. Velegol (2007) Chemotaxis of Nonbiological Colloidal Rods, Phys. Rev. Lett. 99, 178103 (2007).

29 V. Garcia-Gradilla, et al. (2013) Functionalized Ultrasound-Propelled Magnetically Guided Nanomotors: Toward Practical Biomedical Applications, ACS Nano 7, 9232–9240.

30 K. Bente, A. Codutti, F. Bachmann, and D. Faivre (2018) Biohybrid and Bioinspired Magnetic Microswimmers, Small 14, 1704374.

31 I. Tiwari, P. Parmananda, and R. Chelakkot (2020) Periodic oscillations in a string of camphor infused disks, Soft Matter, 2020, DOI: 10.1039/D0SM01393E

32 Y. Fily, P. Subramanian, T.M. Schneider, R. Chelakkot, and A. Gopinath (2020) Buckling instabilities and spatiotemporal dynamics of active elastic filaments, Journal of the Royal Society Interface 17 (165), 20190794.

33 R. Chelakkot, A. Gopinath, L. Mahadevan and M. F. Hagan (2014) Flagellar dynamics of a connected chain of active, polar, Brownian particles, J. Royal Soc. Interface 11 (92), 20130884.

34 G. De Canio, E. Lauga and R. E. Goldstein (2017) Spontaneous oscillations of elastic filaments induced by molecular motors, J. R. Soc. Interface. 14(136), 20170491

35 R. E. Isele-Holder, J. Jager, G. Saggiorato, J. Elgeti and G. Gommpper (2016) Dynamics of self-propelled filaments pushing a load, Soft Matter DOI: 10.1039/c6sm01094f.

36 F. Ling, H. Guo, and E. Kanso (2018) Instability-driven oscillations of elastic microfilaments, J. Royal Soc. Interface, 15(149), 20180594.

37 A. Sangani and A. Gopinath (2020) Elastohydrodynamical instabilities of active filaments, arrays, and carpets analyzed using slender-body theory, Phys. Rev. Fluids 5, 083101.

38 Yi Man and E. Kanso (2020) Multisynchrony in active microfilaments, Phys. Rev. Lett., 125, 148101.

39 R. E. Goldstein, E. Lauga, A. I. Pesci, and M. R. E. Proctor, Elastohydrodynamic synchronization of adjacent beating flagella, Phys. Rev. Fluids 1, 073201 (2016).

40 A. Laskar and R. Adhikari (2017) Filament actuation by an active colloid at low Reynolds number, New J. Phys. 19, 033021.

41 A. K. Manna, P. B. S. Kumar and R. Adhikari (2017) Colloidal transport by active filaments, J. Chem. Phys. 146, 024901.

42 S. Fatehiboroujeni, A. Gopinath and S. Goyal (2018) Nonlinear oscillations induced by follower forces in pre-stressed clamped rods subjected to drag, ASME. J. Comput. Nonlinear Dynamics 13(12), 121005.

43 S. K. Anand, R. Chelakkot and S. P. Singh (2019) Beating to rotational transition of a clamped active ribbon-like filament Soft Matter, 2019,15, 7926-7933.

44 B. Chakrabarti and D. Saintillan (2019) Spontaneous oscillations, beating patterns, and hydrodynamics of active microfilaments, Phys. Rev. Fluids 4, 043102.

45 B. Friedrich (2016) Hydrodynamic synchronization of flagellar oscillators, Eur. Phys. J. Special Topics 225, 2353.

46 N. Uchida, R. Golestanian, and R. R. Bennett (2017) Synchronization and Collective Dynamics of Flagella and Cilia as Hydrodynamically Coupled Oscillators, Journal of the Physical Society of Japan 86, 101007.

47 A. Gopinath and L. Mahadevan (2011) Elastohydrodynamics of wet bristles, carpets and brushes, Proc. Roy. Soc. A., 467(2130), 915 1665.

48 S. Gueron, K. Levit-Gurevich, N. Liron and J. J. Blum (1997) Cilia internal mechanism and metachronal coordination as the result of hydrodynamical coupling, Proc Natl Acad Sci USA 94 (12), 6001.

49 S. Gueron and K. Levit-Gurevich K (1999) Energetic considerations of ciliary beating and the advantage of metachronal coordination, Proc Natl Acad Sci USA 96 (22), 12240.

50 B. Guirao and J. F. Joanny (2007) Spontaneous creation of macroscopic flow and metachronal waves in an array of cilia, Biophys J 92 (6), 1900.

51 C. Wollin and H. Stark (2011) Metachronal waves in a chain of rowers with hydrodynamic interactions, Eur Phys J E Soft Matter, 34(4), 1.

52 J. Elgeti and G. Gompper (2013) Emergence of metachronal waves in cilia arrays, Proc Natl Acad Sci USA 110 (12), 4470.

53 A. Maestro, N. Bruot, Nicolas, J. Kotar, U. Nariya, R. Golestanian and P. Cicuta (2018) Control of synchronization in models of hydrodynamically coupled motile cilia, Communications Physics 1 (1), 1.

54 N. Bruot and P. Cicuta (2016) Realizing the physics of motile cilia synchronization with driven colloids, Annual Review of Condensed Matter Physics 7, 323.

55 L. Damet, G. M. Cicuta, J. Kotar, M. C. Lagomarsino and P. Cicuta (2012) Hydrodynamically synchronized states in active colloidal arrays, Soft Matter 8 (33) 8672.

56 B. Button, L.-H. Cai, C. Ehre, M. Kesimer, D. B. Hill, J. K. Sheehan, R. C. Boucher and M. Rubenstein (2012) A Periciliary Brush Promotes the Lung Health by Separating the Mucus Layer from Airway, Science 337 (6097), 937.

57 Ö. Duman R. E. Isele-Holder, J. Elgeti and G. Gompper (2018) Collective dynamics of self-propelled semiflexible filaments, Soft matter 14(22), 4483–4494.

58 R. E. Isele-Holder, J. Jäger, G. Saggiorato, J. Elgeti and G. Gompper (2016) Dynamics of self-propelled filaments pushing a load, Soft matter 12(41), 8495–8505.

59 R. E. Isele-Holder, J. Elgeti and G. Gompper (2015) Self-propelled worm-like filaments: spontaneous spiral formation, structure, and dynamics, Soft matter 11(36), 7181–7190.

60 A. Gopinath, L. Mahadevan and R. C. Armstrong (2006) Transitions to nematic states in homogeneous suspensions of high aspect ratio magnetic rods, Physics of Fluids 18 (2), 028102.

61 M. Mani, A. Gopinath and L. Mahadevan (2012) How things get stuck: kinetics, elastohydrodynamics, and soft adhesion, Physical review letters 108 (22), 226104.

62 C. Li, B. Qin, A. Gopinath, P. E. Arratia, B. Thomases and R. D. Guy (2017) Flagellar swimming in viscoelastic fluids: role of fluid elastic stress revealed by simulations based on experimental data, Journal of The Royal Society Interface 14 (135), 20170289.